THE EFFECT OF INLET CONDITIONS ON TURBINE ENDWALL LOSS

John D. Coull[1], Christopher J. Clark[2]
[1]University of Oxford, Oxford, UK, [2]University of Cambridge, Cambridge, UK

ABSTRACT

There can be significant variation and uncertainty in the flow conditions entering a blade row. This paper explores how this variability can affect endwall loss in axial turbines.

A computational study of three cascades with collinear inlet boundary layers is conducted. Endwall loss varies by more than a factor of 3 depending on the inlet conditions. This variation is caused by dissipation of Secondary Kinetic Energy (SKE). The results can be understood by observing that the inlet conditions predominantly control how secondary vorticity is distributed within the blade passage. Modestly-thick inlet boundary layers with high shape factor tend to displace vorticity towards the center of the passage. This displacement reduces vorticity cancellation, increasing secondary velocities and SKE.

A general method is formulated to estimate SKE in preliminary design. Optimum aspect ratio is shown to depend on the inlet boundary condition. Strategies to reduce endwall loss and minimize sensitivity to inlet conditions are then highlighted.

1 INTRODUCTION

Endwall flows typically cause one third of the efficiency loss in turbomachines [1]. In axial turbines, these losses are largely generated by dissipation in endwall boundary layers and mixing induced by the secondary flows [2]. These secondary flows arise as the non-uniform inlet flow turns through the blade passage, generating streamwise "secondary" vorticity and bulk flow rotation. In addition a number of discrete vortical structures form, notably the Horse-Shoe Vortex (HSV) system. Reviews of this behavior are given by Sieverding [3] and Langston [4].

This paper examines how the secondary flow and associated losses are affected by the row inflow conditions. In gas turbines these conditions are difficult to predict because they are dependent on the upstream main gas path, secondary air systems, clearances, manufacturing deviations and in-service deterioration. Direct simulation of all possible effects is infeasible, especially during the design process. This paper therefore aims to inform designers by considering:

- Which mechanisms control sensitivity to inlet conditions?
- How are these mechanisms influenced by blade design?

The paper addresses these questions using a computational study of linear cascades, which are ideally suited to detailed analysis of the fundamental mechanisms.

1.1 Previous Studies of Inlet Boundary Conditions

With notable exceptions (e.g. [5]), almost all cascade studies have considered turbulent inlet boundary layers with shape factor $H_{12} \approx 1.3$. In general, net loss tends to increase with boundary layer thickness except for very thick profiles, [6].

Shape factors in turbomachines will tend to be significantly higher than in these cascade tests. The reference frame change between stationary and rotating rows increases the shape factor of the streamwise flow component. This effect is compounded by upstream secondary flows, annulus steps and the injection of low-momentum sealing flows. The available data on shape factor (e.g. [7]) is too sparse to estimate the likely impact on loss.

Thus the starting point for this computational study was to investigate shape factor. For the same inlet boundary layer thickness, Figure 1 shows that increasing H_{12} from 1.3 to 2.6 increases the size and spanwise penetration of the secondary flows, which causes the net mixed-out endwall loss to more than double. The net mass-average loss increases by over 50%.

A wider study for the current cascades showed that shape factor had a generally greater impact on loss than skewed [5] or stage-like [8] inlet conditions. This paper therefore only considers collinear inlet boundary layers.

1.2 The Contribution of Secondary Kinetic Energy

Of the mechanisms that contribute to endwall loss, it is the kinetic energy of the secondary flow that is most sensitive to inlet conditions. Following [9], Figure 2 shows an approximate breakdown of endwall loss components for varying inlet boundary layer thickness δ_{98} and shape factor H_{12}. It can be seen that the variation of net mixed-out loss with inlet conditions is dominated by changes in the Secondary Kinetic Energy (SKE); Denton and Pullan [8] made a similar observation. The majority of the SKE does not dissipate before the trailing edge (TE) plane.

There is significant debate as to what fraction of SKE will be realized as loss in a multistage machine. For these calculations between 40% and 70% of the SKE has already dissipated within half an axial chord of the trailing edge, as the mass-averaged losses in Figure 2 indicate. Denton [1] argues that downstream stages may extract work from the pitch-wise component of the residual SKE, but any recovery of energy will be case-specific and a small fraction of the total. Thus for simplicity this paper assumes that all of the SKE will ultimately be dissipated as loss.

1.3 A Useful Framework to Analyze Secondary Flow

To explain the driving mechanisms, this paper brings together Computational Fluid Dynamics (CFD) simulations and theoretical methods. The analysis shows that it is useful to treat the generation of secondary flow as two distinct processes:

1. The generation of streamwise vorticity, generated by the convection of the inlet flow through the cascade;
2. The induction of secondary velocity and SKE by the vorticity field.

In reality these processes are inter-dependent, i.e. secondary velocity will affect streamwise vorticity generation. Nonetheless this framework is helpful for understanding the key effects.

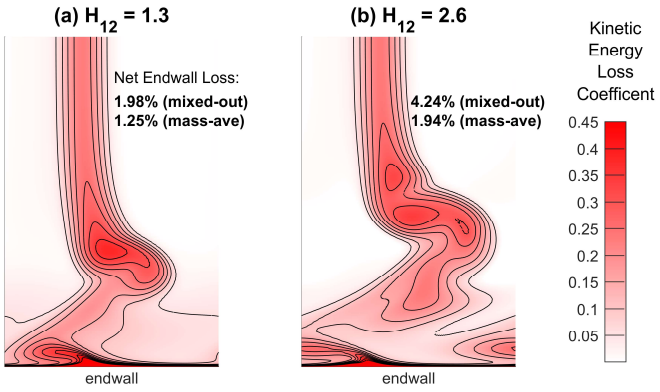

Figure 1: Effect of inlet shape factor on loss: 100° turning cascade, $0.5C_x$ downstream of the trailing edge, $\delta_{98}/p\cos\alpha_2 \approx 0.95$.

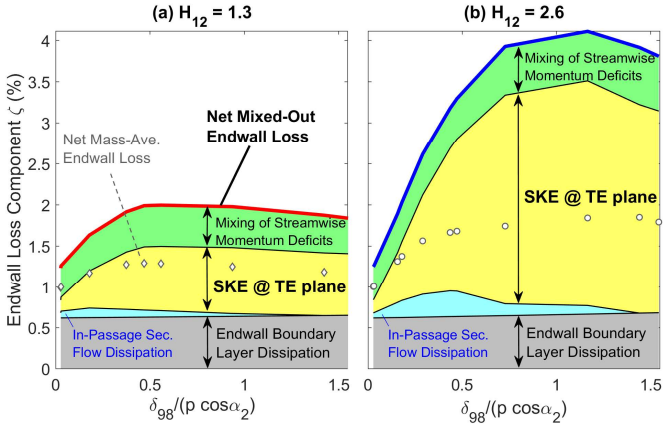

Figure 2: Endwall loss breakdown with varying inlet conditions, 100° turning cascade.

1.4 Secondary Flow Theory

"Classical" secondary flow theory is generally capable of modelling SKE generation, but not the other components of endwall loss. Modelling the convection of inlet vorticity, Squire and Winter [10] argued that secondary vorticity is proportional to turning and used a streamfunction method to calculate the induced secondary velocity field. This paper employs the later refinements of Hawthorne [11], Marsh [12] and others. Inviscid, incompressible flow is considered and the fluid at each spanwise height is assumed to remain in a two-dimensional plane. Thus the theory ignores the inevitable twist and contraction of streamtubes through the blade row. Accounting for these effects complicates the analysis considerably (e.g. [13]).

For a collinear inlet boundary layer, the secondary vorticity ω_{sec} at a given spanwise height is given by (after [11]):

$$\omega_{sec} = \frac{\omega_1}{cos\ \alpha_2}\left(\frac{u_1}{u_2}\frac{C_x}{p}\Delta T^* + \left|sin\ \alpha_1 - \frac{u_1}{u_2}sin\ \alpha_2\right|\right) \qquad (1)$$

The secondary vorticity is thus proportional to the inlet boundary layer (normal) vorticity ω_1 at this height. It is also governed by the inlet and exit flow angles (α_1, α_2), the ratio of streamwise velocities (u_1/u_2), the ratio of pitch to axial chord (p/C_x), and the non-dimensional difference in transit time between flow passing over the pressure and suction surfaces of the blade (ΔT^*). This latter parameter is defined as ([2]):

$$\Delta T^* = \oint \left(\frac{U_2}{U_e}\right) d\left(\frac{S}{C_x}\right) \qquad (2)$$

where U_e is the boundary layer edge velocity, U_2 the row exit velocity at midspan and S the surface length. The integral is performed around the blade perimeter (excluding the singularity at the stagnation point). The transit time is highest when the pressure surface velocity is low, which tends to be the case for designs with higher turning, lower thickness and higher lift [2].

1.5 Paper Outline

The paper is organized as follows:

- Section 2 examines which characteristics of the vorticity field are important for SKE generation;
- Section 3 presents a case study of inlet conditions for three cascades, comparing CFD and secondary flow theory;
- Section 4 examines the key mechanisms;
- Section 5 considers the implications for design.

2 INFLUENCE OF A VORTICITY FIELD ON SKE

In order to set the scene for subsequent analysis, it is helpful to first consider the relationship between the secondary vorticity field and SKE (the second bullet in section 1.3). In particular, which characteristics of the vorticity field determine SKE, and which physical mechanisms control the behavior?

Figure 3 shows a simple model of the flow in the blade passage just upstream of the trailing edge. The passage vorticity is represented by a single streamwise Rankine vortex of circulation Γ and diameter D. For an isolated vortex the induced velocity field is:

$$V_\theta = \begin{cases} \Gamma r/(\pi D^2/2)\,, & r < D/2 \\ \Gamma/(2\pi r)\,, & r \geq D/2 \end{cases} \qquad (3)$$

where r is the distance from the vortex center. In the bounded passage, the velocity field induced by mirror vortices reflected in the endwalls and blades are also superimposed. Numerical calculations are performed for a passage height ($h/2$) to width ($p\cos\alpha_2$) ratio of 3.11 (matching the 100° turning cascade, see below). The five nearest reflected vortices were included, shown in Figure 3, with further mirrors having minimal influence.

The averaged SKE is determined by three factors, the first of which is **Circulation Γ.** The induced velocity from the Rankine and reflected vortices is proportional to Γ, thus for a given diameter and location, SKE is simply proportional to Γ^2.

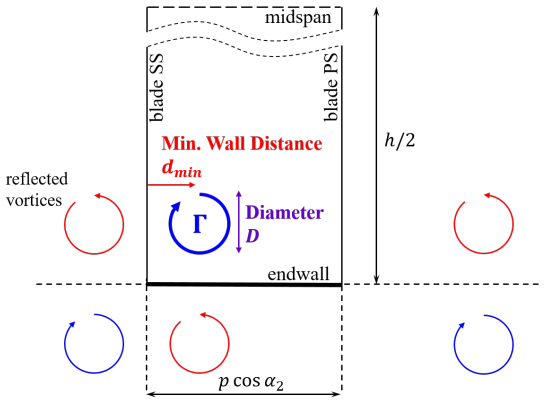

Figure 3: Set-Up of Rankine Vortex Model.

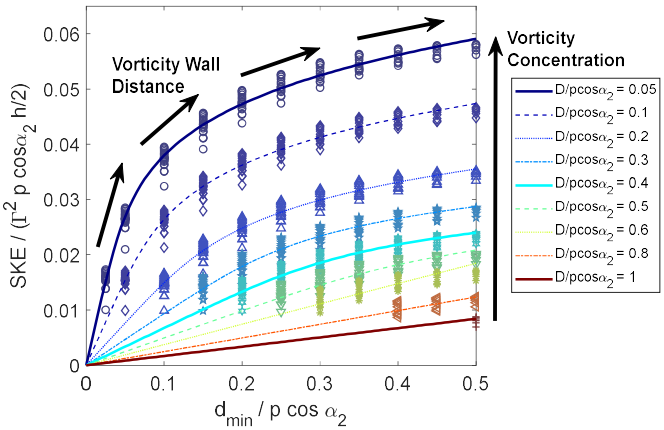

Figure 4: Variation of area-averaged SKE with vorticity distribution in the Rankine Vortex Model.

More subtle are *vorticity distribution effects*, i.e. the vortex position and diameter**.** Calculations with constant Γ and 450 combinations of vortex diameter, horizontal and vertical location are shown in Figure 4. The results show a six-fold variation in the area-averaged SKE, which tends to increase with minimum wall distance d_{min} (Figure 3) and decrease with vortex diameter D. Thus the results show that *vorticity concentrated in the center of the passage* is most damaging for SKE.

Analysis of the model shows that two mechanisms cause the increase of SKE with ***Minimum Wall Distance*** $\boldsymbol{d_{min}}$:

- The first mechanism is independent of the reflected vortices, and thus applies in both bounded and unbounded space. As shown in Figure 5*(a)*, the induced velocity is highest in the near-field of the vortex. As the vortex moves towards the center of the passage (increasing d_{min}), a greater proportion of the high velocity near-field falls within the bounding box of integration, increasing the average SKE.
- The dominant mechanism is Mirror Cancellation. As shown in Figure 5(b), moving the vortex away from the wall (increasing d_{min}) reduces cancellation and increases the average SKE.

The decrease of SKE with ***Vortex Diameter D*** is caused by a third "self-cancelation" mechanism (as distinct from mirror cancellation). As shown in Figure 5(c), increasing D spreads out the constituent elements of the vortex ($\delta\Gamma$). This increases the cancellation between their induced velocity fields and reduces SKE. This effect is akin to decreasing the size of the bounding box (as in (a)), while keeping area-averaged vorticity constant.

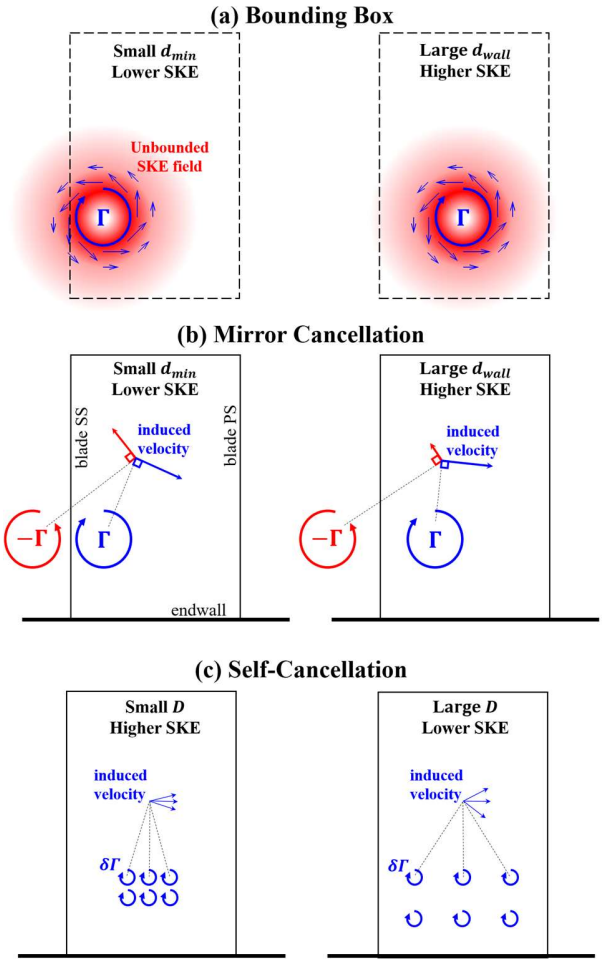

Figure 5: Vorticity distribution mechanisms controlling SKE. For minimum wall distance d_{min}, (b) dominates over (a).

3 A CASE STUDY OF INLET CONDITIONS

Attention now turns to the methods and key results of a computational study of inlet conditions for 3 turbine cascades.

3.1 Turbine Cascades

The three cascades are designed to achieve different flow turning with similar suction surface loading and thickness distributions. Key parameters are given in Table 1. Figure 6(a) compares the geometry and Figure 6(b) presents midspan static pressure coefficients. The designs have similar peak velocity location and level of diffusion on the aft suction surface. The pressure side velocity drops as turning increases, as explained by [2]. The midspan exit Mach number, 0.7, and Reynolds numbers based on axial chord, 200,000, are broadly typical of aero engine low pressure turbines. Apart from the results in section 5.2 the calculations are performed for an aspect ratio of $h/C_x = 3$.

3.2 CFD Calculations

A half-passage domain is simulated with a single viscous endwall and an inviscid wall at midspan. Profiles of stagnation pressure and temperature, angle and turbulence quantities are specified at the inlet, located $0.8C_x$ upstream of the leading edge. A mean static pressure condition is specified at the domain outlet, $1.2C_x$ downstream of the trailing edge. Structured meshes are generated with the Rolls-Royce PADRAM code [14], with a maximum y^+ of around unity on all walls. Each grid has around 10^7 cells, giving good mesh independence as shown in [2].

Steady, fully turbulent Reynolds-Averaged-Navier-Stokes (RANS) calculations are performed using the Rolls-Royce solver HYDRA [15] with the two-equation Shear-Stress-Transport model of Menter [16]. Marconcini et al. [17] have shown that such RANS calculations can predict endwall loss to a similar degree of accuracy as Large Eddy Simulation. This result reflects the largely inviscid

mechanism that produces secondary flow and determines the kinetic energy of the constituent vortices. Figure 7 compares predictions using these CFD methods to endwall loss measured by [7], [18] and [19]. The average error is around 10%, close to the experimental uncertainties.

3.3 Inlet Conditions

Two inlet boundary layer shapes are studied. Figure 8(a) compares normalized velocity for a typical flat-plate turbulent profile and a laminar-like Blausius profile. Figure 8(b) shows the vorticity distributions. The turbulent profile has higher levels of vorticity close to the wall ($z/\delta_{98} < 0.06$) while the laminar-like profile has higher vorticity away from the wall. The product of velocity and vorticity in Figure 8(c) is important for secondary flow generation and will be discussed in section 4.2. Integral parameters of the two profiles are given in Table 2. The freestream turbulent kinetic energy and specific rate of dissipation are chosen to give a turbulence intensity of 5% and a length scale of $0.1C_x$, representative of a multistage turbine [20]. Turbulence parameters for the turbulent boundary layer profile were scaled from a separate flat-plate calculation. For the laminar-like profile, local turbulence intensity was maintained at 5% with a constant specific rate of dissipation; alternative distributions showed minimal effect on the flow field and loss.

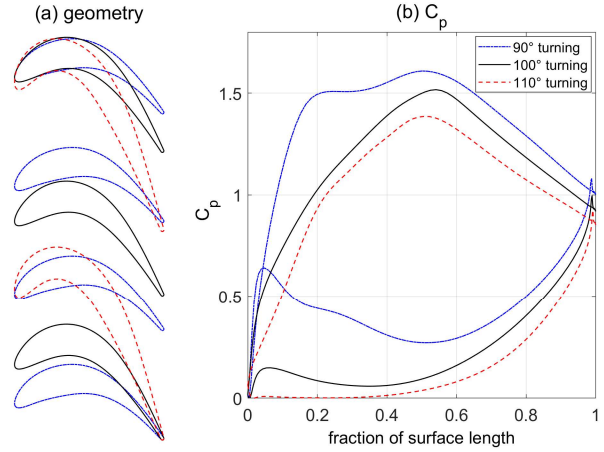

Figure 6: Turbine cascade geometry and pressure distributions.

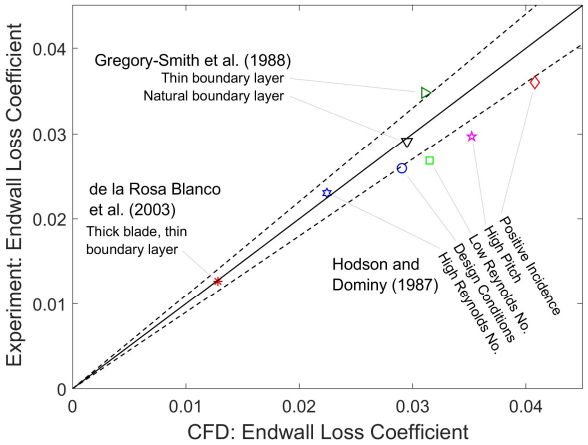

Figure 7: Experimental validation.

Cascade	α_1	α_2	$\frac{U_1}{U_2}$	$\frac{p}{C_x}$	$\frac{h}{p\cos\alpha_2}$	ΔT^*
90° turning	40°	-50°	0.75	0.73	6.40	0.57
100° turning	40°	-60°	0.55	0.96	6.22	1.90
110° turning	40°	-70°	0.36	1.40	6.28	10.12

Table 1 Two-Dimensional cascade design parameters.

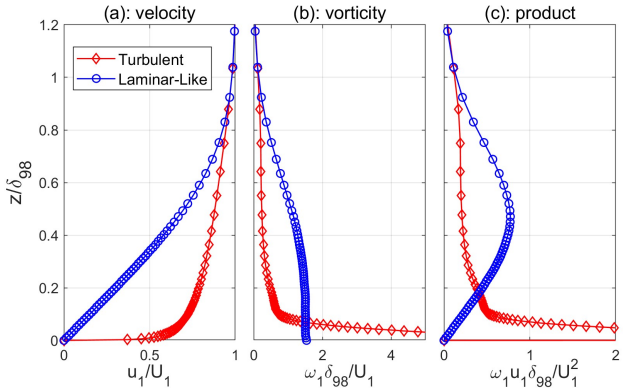

Figure 8: Inlet boundary layer velocity, vorticity and product.

Profile	δ^*/δ_{98}	θ/δ_{98}	H_{12}
Turbulent	0.143	0.111	1.29
Laminar-Like	0.379	0.145	2.62

Table 2 Integral parameters for the inlet boundary layer profiles.

3.4 Definitions of Loss and SKE Coefficients

Kinetic energy loss coefficients are defined by extracting data half an axial chord downstream of the trailing edge. The net passage loss coefficient excludes the inlet loss and is defined as:

$$\zeta_{pass} = \frac{\left(\overline{\overline{u^2}}_{2-is} - u^2_{2-mix}\right)}{\overline{\overline{u^2}}_{2-is}} \tag{4}$$

where $\overline{\overline{u^2}}_{2-is}$ is the mass-averaged square of isentropic exit velocity, calculated from the inlet total and exit static conditions, and u_{2-mix} is obtained from a constant-area mixing calculation of the exit flow to uniform conditions. The passage loss thus includes all future mixing.

The net, mixed-out endwall loss coefficient ζ_{end} is defined in the typical manner by subtracting the profile loss, which is defined using the midspan velocities (U):

$$\zeta_{end} = \zeta_{pass} - \frac{(U^2_{2-is} - U^2_{2-mix})}{U^2_{2-is}} \tag{5}$$

In line with Gregory-Smith et al. [18], secondary velocity components are defined relative to the midspan flow angle at each pitchwise location. The secondary velocity field is extracted at the trailing edge plane, where the majority of the SKE has yet to mix out. The *local* SKE coefficient is given by:

$$SKE^* = \frac{V^2_{norm} + V^2_z}{U^2_{2-is}} \tag{6}$$

where V_z is the spanwise velocity and V_{norm} is the secondary velocity component parallel to the endwall. The mass-averaged SKE coefficient is given by:

$$\zeta_{SKE} = \frac{\overline{\overline{V^2_{norm} + V^2_z}}}{\overline{\overline{u^2}}_{2-is}} \tag{7}$$

3.5 Endwall Loss Variations and the Role of SKE

Figure 9(a-c) show CFD predictions of net mixed-out endwall loss for the three cascades. Several key results are noted:

- Endwall loss is lowest for thin boundary layers and increases by a factor of 3 → 4 depending on the inlet conditions.
- For both inlet profile shapes, increasing the boundary layer thickness δ_{98} causes endwall loss to first rise before plateauing and gradually decreasing. This behavior is consistent with previous studies, e.g. [6], [8].
- Endwall loss for the laminar-like profile (high shape factor) can be more than double that of the turbulent profile.
- Sensitivity to inlet conditions is highest for the higher-turning cascade.

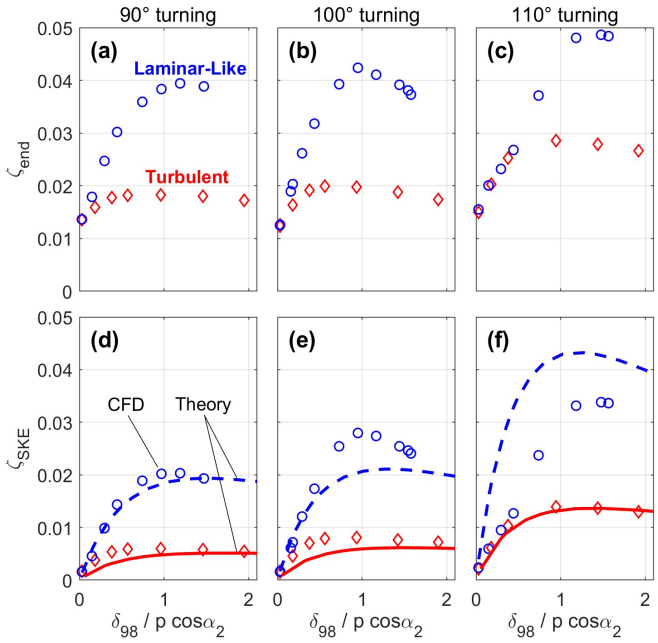

Figure 9: Endwall loss (a-c) and SKE at TE plane (d-f).

Figure 9(d-f) show the SKE coefficients ζ_{SKE}. Comparing with Figure 9(a-c), the variations in SKE closely match the changes in endwall loss with inlet conditions. As previously shown in Figure 2, it is therefore the SKE that drives the sensitivity to inlet conditions.

The classical theory in equation (1) is used to predict the vorticity field for each case, and secondary velocities are calculated using a streamfunction. Details are given in Appendix A. Figure 9(d-f) compares the SKE predictions to the CFD. The discrepancies are generally largest for the laminar-like profiles, which have greater streamtube contraction and twist, and for the 110° turning cascade which has the largest acceleration (Table 1). Nonetheless the theory achieves reasonable quantitative agreement and captures all of the key trends noted above. It can thus be concluded that the theory offers a useful, simplified model that can give insight into the underlying physics.

3.6 Vorticity and SKE Fields

Figure 10 shows CFD predictions of streamwise vorticity at the trailing edge plane for the 100° turning cascade. Two boundary layer thicknesses are shown for both profile shapes. In each case, most of the negatively-signed secondary vorticity rolls up into the Pressure Surface (PS) leg of the Horse Shoe Vortex (HSV) and migrates up the blade Suction Surface (SS). Additional vortex structures are evident such as the counter vortex (positive vorticity close to the SS) and negative vorticity induced by spanwise migration of boundary layer fluid on the blade SS. For a laminar-like, thick boundary layer, Figure 10(d) shows that secondary vorticity is displaced further from the walls (i.e. towards the passage center) compared to the other cases. According to the Rankine model this displacement will cause an increase in SKE, as is observed in Figure 9(e).

The theory in Figure 12 predicts simple distributions of passage vorticity which are uniform across the passage. Nonetheless it will be shown that these distributions possess similar characteristics to the CFD vorticity fields in Figure 10.

The associated secondary flow streamlines and SKE fields are shown in Figure 11 (CFD) and Figure 13 (theory). Clear differences are evident in the details of the secondary flow and the location of high SKE regions, largely due to the lack of streamtube twist in the theory. Nonetheless the global level of SKE responds to inlet conditions in a similar manner to the CFD, as observed in Figure 9(d-f). The Rankine model helps to explain this observation: the detailed vortex structures close to the passage boundaries in Figure 10 have minimal effect on the overall level of SKE because of mirror cancellation (Figure 5(b)). Instead it is the "bulk" characteristics of the vorticity field that control the overall SKE. The following section discusses these effects in detail.

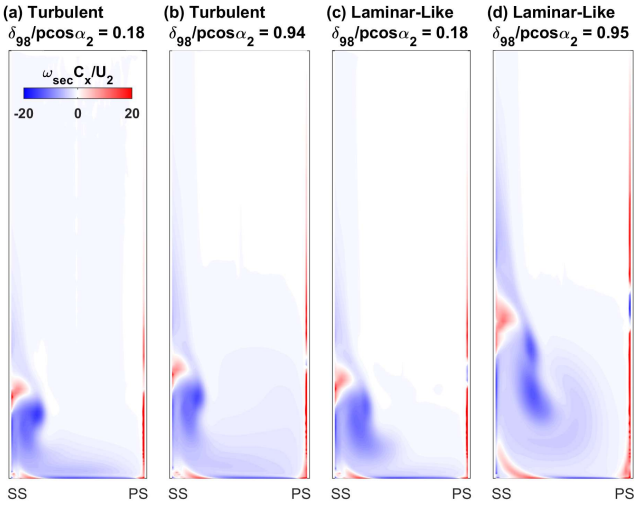

Figure 10: Streamwise vorticity at trailing edge plane, CFD, 100° turning cascade. Negative values associated with passage vortex.

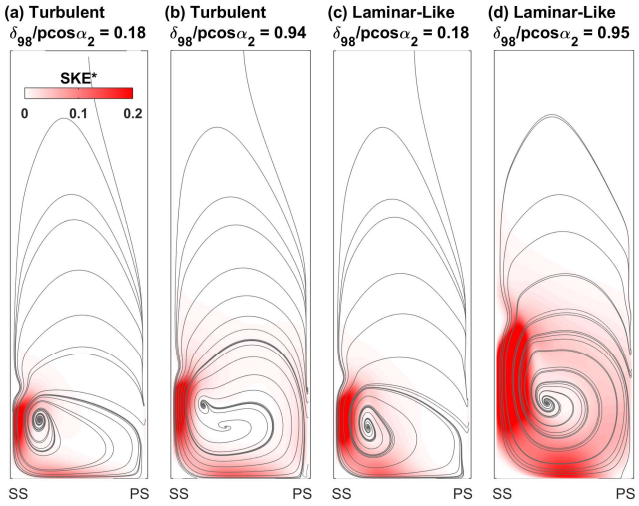

Figure 11: Secondary Kinetic Energy at trailing edge plane, CFD, 100° turning cascade. Same cases as Figure 10.

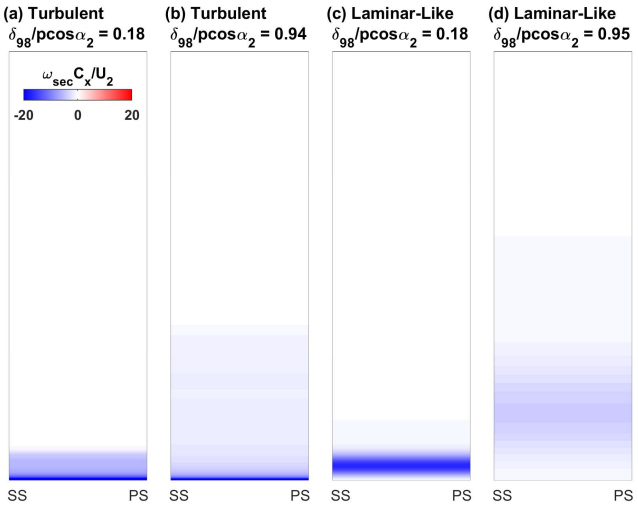

Figure 12: Streamwise vorticity at trailing edge plane, secondary flow theory, 100° turning cascade.

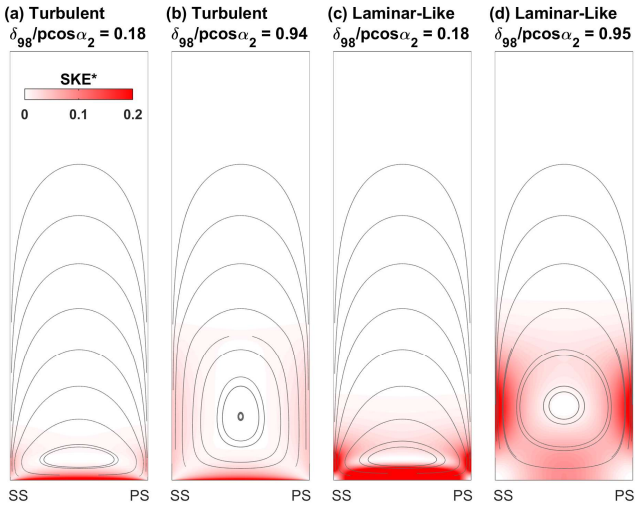

Figure 13: Secondary Kinetic Energy at trailing edge plane, secondary flow theory, 100° turning cascade.

4 KEY MECHANISMS CONTROLLING SKE

This section details the mechanisms driving the variation of SKE with inlet conditions. In line with the Rankine model, the effects of circulation and vorticity distribution are considered.

4.1 Secondary Circulation

By definition, the circulation of the inlet boundary layer (normal) vorticity is simply the freestream velocity U_1. By considering generalized power-law profiles, Appendix B shows that the theory in equation (1) implies that the total secondary circulation Γ_{sec} is also independent of the inlet boundary layer shape and thickness. It is given by the following function of blade design:

$$\frac{\Gamma_{sec}}{U_2 p \cos\alpha_2} = U^* \frac{\Delta T^* C_x}{p \cos\alpha_2} + \left| \frac{U_1}{U_2} \frac{\sin\alpha_1}{\cos\alpha_2} - U^* \tan\alpha_2 \right| \quad (8)$$

where:

$$U^* = \left(1 - \sqrt{1 - (U_1/U_2)^2}\right) \qquad (9)$$

Substituting values for the 3 cascades (Table 1) shows that circulation increases with turning: $\Gamma_{sec}/U_2 p\cos\alpha_2$ =1.55, 1.63 and 2.28 for the 90°, 100° and 110° turning cascades respectively. This increase is driven by the increase in transit time ΔT^* with turning for these three designs: higher turning increases cross-passage pressure gradients [2], tending to depress the pressure side velocity as in Figure 6(b). This change in circulation explains why the theory predicts an increase in SKE with turning for the three cascades, Figure 9(d-f).

The behavior of the CFD is more complex than the theory, but the first-order trends are consistent. As in the Rankine model, Figure 14(a) shows SKE normalized with the square of the theoretical circulation (equation (8)) and the passage area:

$$\Pi_{SKE} = \frac{\zeta_{SKE}\left(\frac{h}{2} p\cos\alpha_2\right)}{\Gamma_{sec}^2/U_2^2} \qquad (10)$$

The Π_{SKE} parameter is a function of the *vorticity distribution alone* and is discussed further in section 5.1. Figure 14(a) collapses the CFD data for the three cascades within a spread of ±10% for the turbulent profile and ±20% for the laminar-like profile. The greater spread in the latter case is consistent with the errors in Figure 9(d-f) and is in part due to greater streamtube contraction when the inlet shape factor is high. The collapse for the theoretical results in Figure 14(b) is much closer.

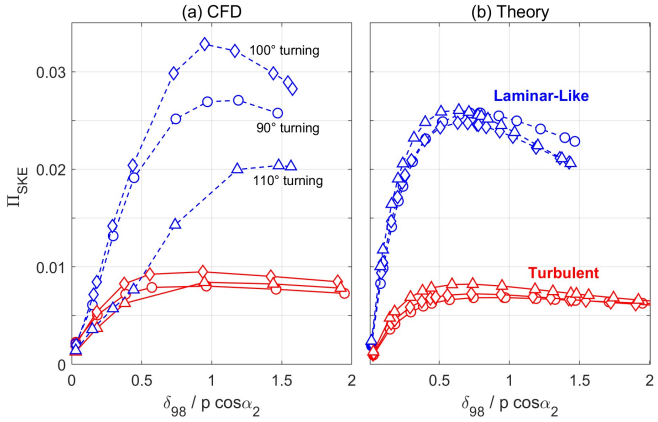

Figure 14: SKE normalized using theoretical circulation (eq. (10)).

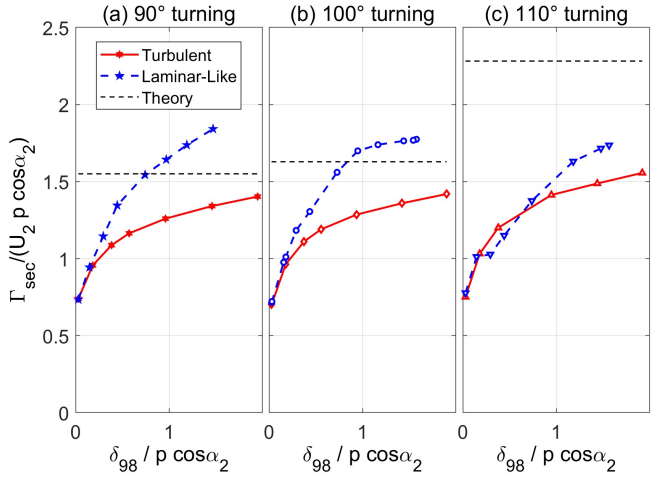

Figure 15: Secondary Circulation predicted by CFD.

The secondary circulation in the 3D CFD is only loosely correlated to the theory because of its simplifying assumptions. The largest difference is caused by viscous dissipation, which has the greatest effect in regions of high velocity gradients i.e. high vorticity. In general these regions are close to the passage walls where the vorticity has little impact on SKE (section 2). Thus the CFD shows generally lower secondary circulation, but the differences are not important for SKE.

Figure 15 presents circulation calculated by integrating negative streamwise vorticity at the trailing edge from CFD. The circulation is lowest for thin inlet boundary layers when the flow spatial gradients (and so dissipation) are greatest. The CFD also shows a smaller

increase in circulation with turning than the theory, again indicating increasing viscous dissipation when secondary velocities are largest, i.e. for the 110° turning cascade. This effect was observed for a large number of cascades in [9].

4.2 Vorticity Distribution Effects

Normalized SKE (Π_{SKE}, Figure 14) varies with inlet conditions due to vorticity distribution effects. These can be quantified by considering equivalents to the wall distance d_{min} and diameter D in the Rankine model in section 2:

Vorticity Wall Distance $\delta_{\omega-min}$. For each location in the trailing edge plane the distance to the closest boundary wall (d_{min}, Figure 3), is evaluated in the plane perpendicular to the bulk primary flow (α_2) direction. The average vorticity wall distance is then defined by integration across the passage:

$$\delta_{\omega-min} = \frac{\iint \omega_{sec} d_{min}\, \mathrm{d}y^* dz}{\iint \omega_{sec}\, \mathrm{d}y^* dz} \qquad (11)$$

Only the negative vorticity associated with the passage vortex is considered, and $y^* = y \cos\alpha_2$ is normal to the primary flow (see Figure 20). Thus $\delta_{\omega-min}$ is a vorticity-weighted wall distance.

Vorticity Integral Diameter D'. An equivalent vortex diameter is defined by calculating an integral diameter from the two-dimensional autocorrelation R of the (negatively-signed) vorticity field (Figure 10):

$$D' = \sqrt{\iint R\, dy^* dz} \qquad (12)$$

The integral is performed over the entire range of the autocorrelation. This approach is analogous to the calculation of turbulence integral time and length scales from a hot-wire signal.

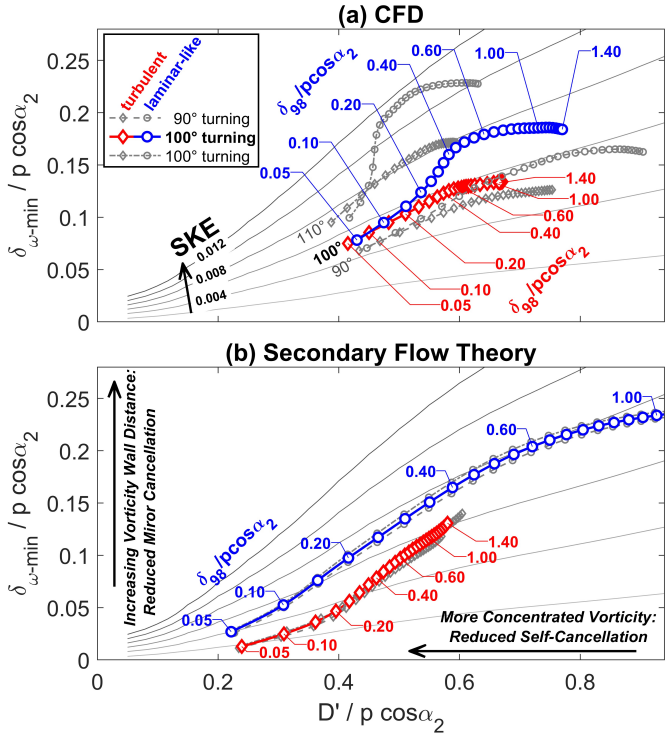

Figure 16: Vorticity distribution effects: vorticity wall distance $\delta_{\omega-min}$ and effective vorticity diameter D'. Contours of normalized SKE from the Rankine model in section 2.

Figure 16(a) shows D' and $\delta_{\omega-min}$ as inlet conditions vary. Each line interpolates between the CFD results, and symbols show increments of $\delta_{98}/p\cos\alpha_2 = 0.05$. The three cascades show similar trends for the turbulent and laminar-like inlet profiles. The theory in Figure 16(b) shows similar qualitative behavior. Considering first the 100° turning cascade, it can be seen that:

- Increasing δ_{98} increases both vorticity wall distance $\delta_{\omega-min}$ and integral diameter D'. These effects *simply mimic the distribution of inlet vorticity,* which displaces away from the wall and becomes more diffuse as δ_{98} increases. Maximum SKE occurs when the opposing effects of $\delta_{\omega-min}$ and D' are balanced.
- Increasing inlet shape factor (turbulent → laminar-like) predominantly increases $\delta_{\omega-min}$ and thus reduces mirror cancellation (Figure 5(b)). This increase in wall distance is also evident in the contour plots in Figure 10 and Figure 12.

The theory also explains why increasing shape factor moves vorticity away from the wall (increasing $\delta_{\omega-\min}$). This effect is driven by the dependency of secondary vorticity on the product of inlet vorticity and velocity, $\omega_1 u_1$, for two of the three terms in equation (1). As shown in Figure 8(c), this product is a maximum at the wall for the turbulent profile but peaks at around $z/\delta_{98} \approx 0.6$ for the laminar-like profile. This shift reflects a more gradual increase in velocity and decrease in vorticity with height for the laminar-like profile.

The differences between the 3 designs are also noteworthy. The theory in Figure 16(b) shows near-identical behavior, while the CFD results in Figure 16(a) show that higher-turning designs tend to have higher wall distance and smaller diameter. This result reflects the increase in strength of the secondary flows with higher turning. First, stronger secondary flows roll-up more readily, tending to concentrate vorticity (lower D') away from the walls (higher $\delta_{\omega-min}$). Second, as noted above, stronger secondary flows will cause higher viscous dissipation which largely attenuates vorticity in the near-wall regions. Thus the remaining vorticity is more concentrated towards the passage center (higher wall distance) for the higher turning cascade.

5 DESIGN AND PERFORMANCE IMPLICATIONS

The implications for turbine design and performance are now considered. Two practical questions are considered:

- How can SKE be predicted in the general case?
- How can SKE and sensitivity to inlet conditions be reduced?

5.1 Universal Scaling including Aspect Ratio

Several studies show that endwall loss varies inversely with span, but it will be shown that this is only strictly true when inlet conditions scale with the blade chord and pitch. Most authors consider a non-dimensional aspect ratio of span-to-axial-chord (h/C_x), but the current analysis demonstrates that the ratio of span to the effective exit passage width, $h/p\cos\alpha_2$, is more fundamental. This definition is close to the span-to-throat ratio used in the correlation of Craig and Cox [21].

Streamfunction calculations (Appendix A) are performed for the 100° turning cascade with multiple power-law inlet profiles (equation (B3)). Maintaining the distribution of ω_{sec} as a fraction of span, the domain pitch ($p\cos\alpha_2$) and height ($h/2$) are then systematically set to 50%, 100% and 200% of their original values, giving 9 different domain sizes. The results collapse to the following relationship, as in equation (10):

$$\zeta_{SKE} \approx 2\left(\frac{p\,cos\,\alpha_2}{h}\right)\left[\frac{\Gamma_{sec}}{U_2 p\,cos\,\alpha_2}\right]^2 \Pi_{SKE} \qquad (13)$$

The factor 2 on the right-hand-side arises reflects contributions from both endwalls. The other three factors respectively capture:

1. The inverse aspect ratio ($p\,cos\,\alpha_2\,/h$), set by 3D design.
2. The square of non-dimensional secondary circulation, a function of the 2D section design only (equation (8)).
3. The effects of vorticity distribution, Π_{SKE}.

As Figure 17 shows, the latter parameter is a function of inlet conditions:

$$\Pi_{SKE} = f\left(\frac{\delta_{98}}{p\,cos\,\alpha_2}, H_{12}\right) \qquad (14)$$

Three regimes are indicated on Figure 17. For thin boundary layers ($\delta_{98}/p\,cos\,\alpha_2 < \sim 0.1$), Π_{SKE} increases proportionally with the boundary layer thickness, driven by increasing vorticity wall distance $\delta_{\omega-min}$. A buffer region separates this regime from the thick boundary layer regime, where SKE drops with increasing δ_{98} due to increasing vorticity diameter D'. The case of linear profiles ($n = 1$) agrees with Hawthorne's analysis [22].

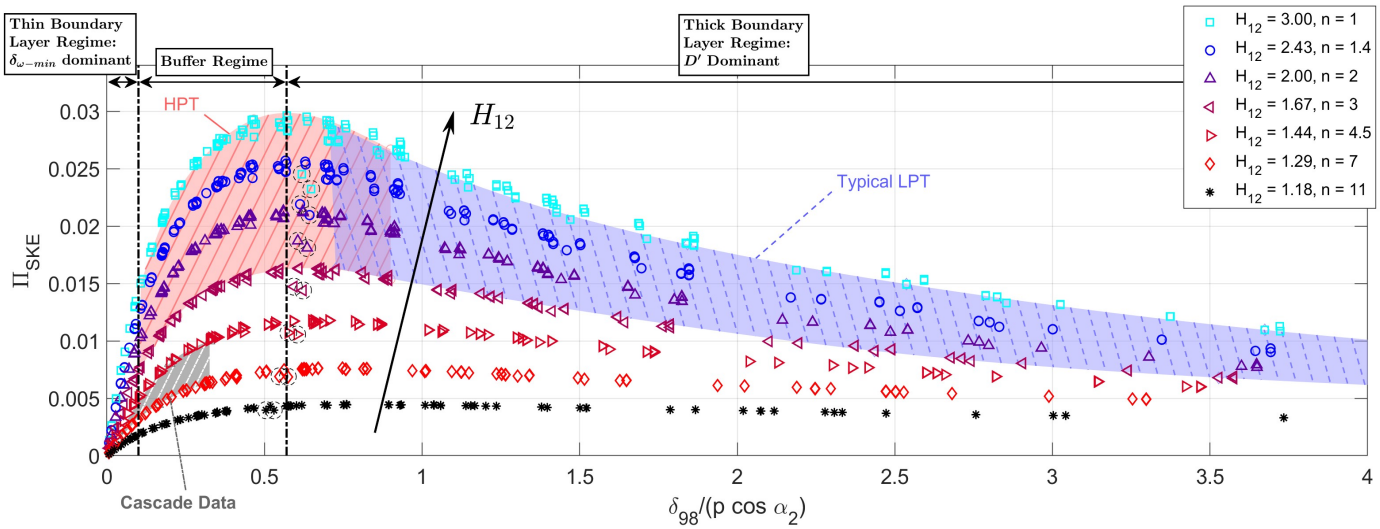

Figure 17: Vorticity Distribution function Π_{SKE} and flow regimes, from secondary flow theory calculations. Hatched areas indicative approximate ranges for gas turbine stages and cascade data. (Circled outliers are low aspect ratio cases with midspan vorticity reflection.)

The plot also includes approximate ranges for aero engine High Pressure Turbines (HPT), Low Pressure Turbines (LPT) and cascade experiments in the literature. It can be seen that:

- Π_{SKE} is generally higher for engines than cascade studies predominantly due to higher shape factor. This observation partly explains why endwall loss is typically much higher in engines than cascades.
- Π_{SKE} is generally highest for HPTs. LPTs generally have small chord and pitch, pushing $\delta_{98}/p\,cos\,\alpha_2$ into the thick boundary layer regime where Π_{SKE} is lower.
- There may be significant scope to reduce SKE in engines, as discussed in section 5.3.

Together with equation (13), Figure 17 enables SKE to be estimated for any cascade with a collinear inlet boundary layer.

5.2 Example: Aspect Ratio Selection

To illustrate the implications of the above method, a simple preliminary design problem is considered. As shown in Figure 18, a parallel duct of fixed height h has a given inlet boundary layer height δ_{98} and shape factor H_{12}. The blade 2D design, and thus pitch-to-chord ratio, is fixed. The designer must select the blade axial chord, which sets the pitch and thus the aspect ratio $h/p\,cos\,\alpha_2$. The 100° turning cascade profile is used and for simplicity only the SKE contribution to loss is considered.

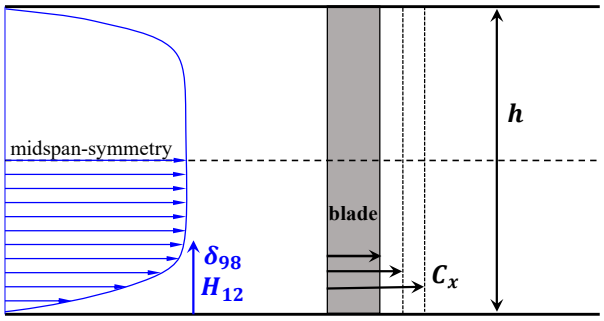

Figure 18: Aspect Ratio Study.

For different ratios of boundary layer thickness to span δ_{98}/h, Figure 19 shows how SKE varies with inverse aspect ratio for (a) turbulent and (b) laminar-like inlet profiles. Symbols show CFD calculations and lines show estimates from Figure 17 and equation (13). In general the estimates give similar trends and levels to the CFD, with SKE typically 3 times higher for the laminar-like profiles. Errors in the estimates for individual cases are in line with Figure 9(e): the turbulent case is more closely predicted and there is a wider spread for the laminar-like profile.

For thin boundary layers ($\delta_{98}/h \approx 0.005$), Figure 19 shows that SKE is almost insensitive to aspect ratio. This behavior occurs because Π_{SKE} is roughly proportional to $\delta_{98}/p\cos\alpha_2$ in the thin boundary layer regime (Figure 17). From equation (13):

$$\zeta_{SKE} \propto \left(\frac{p\,cos\,\alpha_2}{h}\right)\left(\frac{\delta_{98}}{p\cos\alpha_2}\right) = \frac{\delta_{98}}{h} \qquad (15)$$

For thick inlet boundary layers ($\delta_{98}/h = 0.25$), Figure 19 shows that SKE tends to increase more rapidly with $p\,cos\,\alpha_2\,/h$ than a simple inverse relationship. This trend occurs because increasing $p\cos\alpha_2$ reduces $\delta_{98}/p\cos\alpha_2$, thus increasing Π_{SKE} (the thick boundary layer regime in Figure 17). Thus vorticity distribution effects compound the influence of aspect ratio.

This simple exercise does not include other components of loss, for example endwall boundary layer dissipation which is inversely proportional to aspect ratio [2]. Nonetheless it demonstrates that the choice of optimal aspect ratio will depend on the inlet conditions of the installed blade row.

5.3 Strategies to Reduce Loss

The findings highlight means to reduce SKE and sensitivity to inlet conditions.

First, the secondary circulation (equation (8)) can be reduced by careful blade design. For given flow angles, this can be achieved by increasing pressure surface velocities to reduce the transit time difference ΔT^*. This will require thickening of blade profiles in the endwall region (e.g. as demonstrated by [7]), careful choice of lift coefficient, and trade-off with profile loss.

Second, estimates of inlet conditions should be used to choose a more optimal aspect ratio in preliminary design.

Third, careful design of upstream components and seal geometries should be used to control the inlet conditions. Reducing the shape factor of the streamwise flow component can be expected to be particularly beneficial.

Finally, the analysis sheds new light on secondary flow control methods, such as endwall contouring and fences. In general such methods help to control the trajectory of vortical structures in the passage. The current analysis shows that these approaches will be most effective at minimizing SKE when they move these vortices towards the passage walls, and ideally the corners, in order to maximize mirror cancellation (Figure 5(b)).

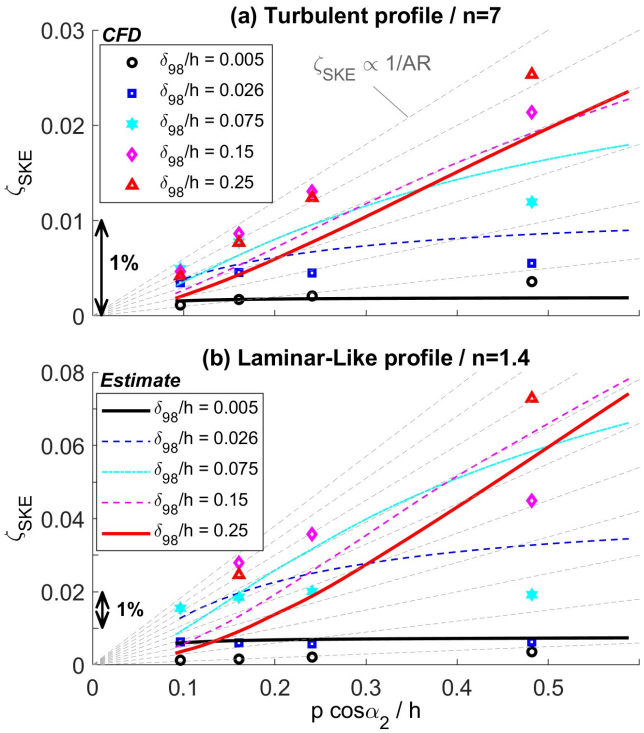

Figure 19: SKE vs. Inverse Aspect Ratio (AR) for different inlet conditions, 100° turning cascade. Symbols are CFD, lines show preliminary design estimates using Figure 17 and eq. (13).

6 CONCLUSIONS

A CFD study of turbine cascades has shown that net endwall loss can vary by more than a factor of 3 depending on the inlet conditions, tending to be highest when the inlet shape factor is high and boundary layer thickness is of the order of the throat width. These variations in endwall loss are driven by an order-of-magnitude variation in Secondary Kinetic Energy (SKE).

Classical secondary flow theory reproduces the SKE trends of the CFD study to a reasonable degree of accuracy. The theory predicts that overall secondary circulation depends only on blade design, tending to increase with blade turning. In contrast, inlet conditions affect loss by controlling *the distribution of vorticity* within the passage. The CFD results are more complex than the theory but exhibit similar characteristics.

Two global characteristics of the vorticity distribution affect SKE generation:

1) Vorticity Wall Distance: As inlet boundary layer thickness and shape factor increase, secondary vorticity moves away from the passage walls. The increased wall distance reduces cancelation with reflected vorticity and increases the global level of SKE.
2) Vorticity Concentration: Thicker inlet boundary layers cause the secondary vorticity to become more diffuse. This effect reduces SKE by increasing cancellation between the constituent elements of the vorticity field.

SKE is thus largest for high shape factor and moderate inlet boundary layer thickness, when these two mechanisms balance.

A generalized preliminary design method for estimating SKE has been formulated and demonstrates that the choice of optimal blade aspect ratio depends on the inlet conditions. For very thin inlet boundary layers SKE is insensitive to aspect ratio.

The analysis highlights opportunities to reduce endwall loss and sensitivity to inlet conditions, in particular by increasing pressure side velocities to reduce secondary circulation.

ACKNOWLEDGEMENTS

Funding from Rolls-Royce plc. is gratefully acknowledged. The authors would like to thank Ed Greitzer, Nick Cumpsty, Howard Hodson, John Denton, Colin Scrivener, Frederic Goenaga and Raul Vazquez for their comments.

NOMENCLATURE

Symbols

C_x	axial chord
d_{min}	vorticity minimum wall distance
D	Rankine vortex diameter
D'	equivalent diameter for distributed vorticity (eq. (12))
h	span
H_{12}	shape factor $= \delta^*/\theta$
p	pitch
R	two-dimensional autocorrelation of vorticity
S	surface distance
SKE^*	local Secondary Kinetic Energy (eq. (6))
U	freestream velocity
V	velocity
V_{norm}	in-plane secondary velocity
W	spanwise velocity
x	axial coordinate
y	pitchwise coordinate
y^*	pitchwise coordinate normal to the exit flow $= y\cos\alpha_2$
z	spanwise coordinate
α	pitchwise flow angle
Γ	circulation
δ_{98}	boundary layer thickness for $V = 0.98U$
δ^*	displacement thickness
$\delta_{\omega-min}$	vorticity-weighted minimum wall distance (eq. (11))
ΔT^*	non-dimensional transit time difference (eq. (2))
ζ	loss coefficient
θ	momentum thickness
Π_{SKE}	vorticity distribution factor (eq. (10))
ψ	streamfunction
ω	vorticity

Subscripts and Abbreviations

1	inlet
2	outlet

e	boundary layer edge (freestream)
end	endwall
$pass$	passage
PS	Pressure Surface
sec	secondary
SKE	Secondary Kinetic Energy
SS	Suction Surface

REFERENCES

[1] Denton, J.D., 1993, Loss Mechanisms In Turbomachines. *J. Turbomach*., **115**(4), pp. 621-656.
[2] Coull, J.D., 2017, Endwall Loss In Turbine Cascades, *J. Turbomach.* **139**(8) pp. 081004
[3] Sieverding, C.H. 1985, Recent Progress In The Understanding Of Basic Aspects Of Secondary Flows In Turbine Blade Passages. *J. Eng. Gas Turbines Power* **107**(2) Pp. 248-257
[4] Langston, L.S., 2001, "Secondary Flows In Axial Turbines—A Review" *Annals Of The New York Academy Of Sciences* 934.1 (2001) pp. 11-26
[5] Walsh, J. and Gregory-Smith, D.G., 1990. Inlet skew and the growth of secondary losses and vorticity in a turbine cascade. *Journal of Turbomachinery*, *112*(4), pp.633-642.
[6] Dunham, J., 1970. A review of cascade data on secondary losses in turbines. *Journal of Mechanical Engineering Science*, *12*(1), pp.48-59
[7] de la Rosa Blanco, E.R., Hodson, H.P., Vazquez, R. and Torre, D., 2003, Influence Of The State Of The Inlet Endwall Boundary Layer On The Interaction Between Pressure Surface Separation And Endwall Flows. *Proceedings Of The Institution Of Mechanical Engineers, Part A: Journal Of Power And Energy*, **217**(4), Pp.433-441.
[8] Denton, J. and Pullan, G., 2012, A Numerical Investigation Into The Sources Of Endwall Loss In Axial Flow Turbines. *ASME Paper GT2012-69173*
[9] Coull, J.D., Clark, C.J. and Vazquez, R., 2019, The Sensitivity of Turbine Cascade Endwall Loss To Inlet Boundary Layer Thickness. *Journal of the Global Power and Propulsion Society **3***
[10] Squire, H.B. and Winter, K.G., 1951, The Secondary Flow In A Cascade Of Airfoils In A Nonuniform Stream. *Journal of the Aeronautical Sciences,* **18**(4), pp.271-277
[11] Hawthorne, W.R., 1955, Rotational Flow Through Cascades: Part 1: The Components Of Vorticity. *Quart. Journ. Mech. and Applied Math.* **8**(3)
[12] Marsh, H., 1976, Secondary Flow In Cascades – The Effect Of Compressibility, *Aeronautical Research Council R&M* No. 3778
[13] Okan, B.M. and Gregory-Smith, D.G., 1995, The Estimation Of Secondary Flows And Losses In Turbines. *VDI Berichte*, **1185**, pp.127-127
[14] Shahpar, S., and Lapworth, L., 2003, PADRAM: Parametric Design And Rapid Meshing System For Turbomachinery Optimisation. *ASME Turbo Expo 2003*, GT2003-38698
[15] Moinier, P., and Giles, M.B., 1998, Preconditioned Euler and Navier-Stokes Calculations On Unstructured Grids. *6th ICFD Conference On Numerical Methods For Fluid Dynamics, Oxford, UK*
[16] Menter, F.R., 1994, Two-Equation Eddy-Viscosity Turbulence Models For Engineering Application. *AIAA Journal,* **32**(8), Pp. 1598-1605
[17] Marconcini, M., Pacciani, R., Arnone, A., Michelassi, V., Pichler, R., Zhao, Y. and Sandberg, R., 2019. Large Eddy Simulation and RANS Analysis of the End-Wall Flow in a Linear Low-Pressure-Turbine Cascade - Part II: Loss Generation. *J. Turbomach*. **141**(5)
[18] Gregory-Smith, D.G., Graves, C.P., and Walsh, J.A., 1988, Growth Of Secondary Losses And Vorticity In An Axial Turbine Cascade. *J. Turbomach.,* **110**(1), pp. 1-8
[19] Hodson, H.P. and Dominy, R.G., 1987, "The Off-Design Performance Of A Low-Pressure Turbine Cascade" Asme. *J. Turbomach.,* **109**(2), pp. 201-209
[20] Halstead, D.E., 1996, Boundary Layer Development In Multi-Stage Low Pressure Turbines. *PhD Thesis, Iowa State University*
[21] Craig, H.R.M., and Cox, H.J.A., 1971, Performance Estimation Of Axial Flow Turbines, *Proc. I. Mech. E.,* 185(32/71), 1970-71
[22] Hawthorne, W.R., 1955. *Some formulae for the calculation of secondary flow in cascades*. Aeronautical Research Council.

APPENDIX A: APPLICATION OF THEORY

Equation (1) is applied at each spanwise height. Figure 20 shows the nomenclature and coordinate system. As in the CFD, a half-span cascade is considered. The primary flow exit angle α_2 is assumed constant and equal to the freestream value, and the velocity $u_2(z)$ is the isentropic value, calculated by considering the kinetic energy deficit of the incoming boundary layer fluid:

$$\frac{1}{2}(U_2^2 - u_2^2) = \frac{1}{2}(U_1^2 - u_1^2) \qquad \text{(A1)}$$

An alternative method to calculate u_1/u_2 is to apply continuity to each slice but this gives unrealistically high SKE.

The secondary velocities $V_{norm}(y,z)$ and $W(y,z)$ are normal to α_2, and are calculated using a streamfunction ψ [10]:

$$W = \frac{d\psi}{dy^*},\ V_{norm} = -\frac{d\psi}{dz} \qquad \text{(A2)}$$

V_{norm} and y^* are the velocity and distance perpendicular to the primary flow, see Figure 20. The streamfunction is calculated numerically from the vorticity given by equation (1), after [10]:

$$\frac{\partial^2\psi}{\partial y^{*2}} + \frac{\partial^2\psi}{\partial z^2} = -\omega_{sec} \qquad \text{(A3)}$$

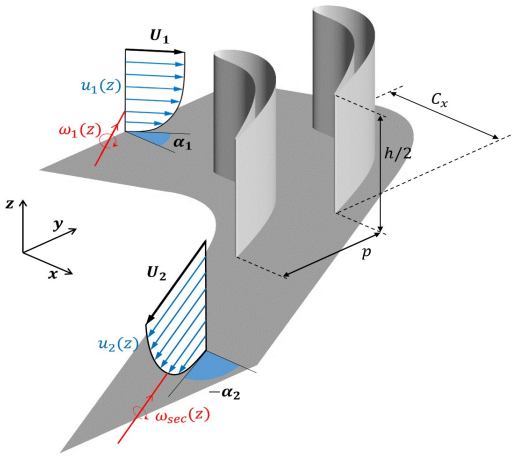

Figure 20 Definitions for application of secondary flow theory.

APPENDIX B: SECONDARY CIRCULATION

The circulation of the secondary vorticity, Γ_{sec}, is equal to the area-integral of ω_{sec} across the passage:

$$\Gamma_{sec} = \iint \omega_{sec} dy^* dz = (p\cos\alpha_2)\left(\frac{h}{2}\right)\overline{\omega_{sec}} \qquad \text{(B1)}$$

where the over-bar indicates area averaging. From equation (1), the area-average secondary vorticity is given by:

$$\overline{\omega_{sec}} = \left\{\frac{\overline{\omega_1 u_1}}{u_2}\right\}\frac{C_x \Delta T^*}{p\cos\alpha_2} + \left|\{\overline{\omega_1}\}\frac{\sin\alpha_1}{\cos\alpha_2} - \left\{\frac{\overline{\omega_1 u_1}}{u_2}\right\}\tan\alpha_2\right| \qquad \text{(B2)}$$

For a power-law profile, velocity and vorticity are given by:

$$\frac{u_1}{U_1} = \begin{cases} \left(\frac{z}{\delta}\right)^{1/n}, & z \le \delta \\ 1, & z > \delta \end{cases} \qquad \text{(B3)}$$

$$\omega_1 = \begin{cases} \frac{U_1}{n\delta}\left(\frac{z}{\delta}\right)^{\frac{1-n}{n}}, & z \le \delta \\ 0, & z > \delta \end{cases} \qquad \text{(B4)}$$

The area-average inlet vorticity in equation (B2) is thus:

$$\overline{\{\omega_1\}} = \frac{2}{h}\frac{U_1}{n\delta}\int_0^\delta \left(\frac{z}{\delta}\right)^{\frac{1-n}{n}} dz = \frac{U_1}{(h/2)} \qquad \text{(B5)}$$

From equation (A1), the outlet velocity is given by:

$$\frac{u_2}{U_2} = \begin{cases} \sqrt{1 - \left(\frac{U_1}{U_2}\right)^2\left(1 - \left(\frac{z}{\delta}\right)^{\frac{2}{n}}\right)}, & z \le \delta \\ 1, & z > \delta \end{cases} \qquad \text{(B6)}$$

Thus for $z \leq \delta$ the product of inlet vorticity and velocity ratio is:

$$\frac{\omega_1 u_1}{u_2} = \frac{U_1}{n\delta}\left(\frac{U_1}{U_2}\right)\left(\frac{z}{\delta}\right)^{\frac{2-n}{n}}\left(1-\left(\frac{U_1}{U_2}\right)^2\left(1-\left(\frac{z}{\delta}\right)^{\frac{2}{n}}\right)\right)^{-0.5} \qquad \text{(B7)}$$

The average can be obtained by integration:

$$\overline{\left\{\omega_1 \frac{u_1}{u_2}\right\}} = \frac{2}{h}\int_0^{\delta} \frac{\omega_1 u_1}{u_2} dz = \frac{U_2}{(h/2)}\left(1-\sqrt{1-\left(\frac{U_1}{U_2}\right)^2}\right) \qquad \text{(B8)}$$

Substituting equations (B5) and (B8) into (B2), and then $\overline{\omega_{sec}}$ into equation (B1) gives the result in equation (8) in the main text.